https://doi.org/10.1007/s41230-025-4048-7

Optimization of laser cladding FeMnSiCrNi memory alloy coating process based on response surface model and NSGA-2 algorithm

Yu Zhang[1], *Guang-lei Liu[1, 2], Shu-cong Liu[1], Wen-chao Xue[1], Wei-mei Chen[1], Hai-xia Liu[1], and Jian-zhong Zhou[2]

1. School of Materials Science and Engineering, Jiangsu University, Zhenjiang 212013, Jiangsu, China

2. School of Mechanical Engineering, Jiangsu University, Zhenjiang 2120013, Jiangsu, China

Abstract: To solve the problems of deformation, micro-cracks, and residual tensile stress in laser cladding coatings, the technique of laser cladding with Fe-based memory alloy can be considered. However, the process of in-situ synthesis of Fe-based memory alloy coatings is extremely complex. At present, there is no clear guidance scheme for its preparation process, which limits its promotion and application to some extent. Therefore, in this study, response surface methodology (RSM) was used to model the response surface between the target values and the cladding process parameters. The NSGA-2 algorithm was employed to optimize the process parameters. The results indicate that the composite optimization method consisting of RSM and the NSGA-2 algorithm can establish a more accurate model, with an error of less than 4.5% between the predicted and actual values. Based on this established model, the optimal scheme for process parameters corresponding to different target results can be rapidly obtained. The prepared coating exhibits a uniform structure, with no defects such as pores, cracks, and deformation. The surface roughness and microhardness of the coating are enhanced, the shaping quality of the coating is effectively improved, and the electrochemical corrosion performance of the coating in 3.5% NaCl solution is obviously better than that of the substrate, providing an important guide for engineering applications.

Keywords: laser cladding; shape memory alloy coating; response surface method; process parameters optimization; NSGA-2 algorithm

CLC numbers: TG142 **Document code:** A **Article ID:** 1672-6421(2025)03-311-12

1 Introduction

As a deep integration and extension of repair and manufacturing technologies, remanufacturing technology is highly flexible and rapid. A large number of issues related to equipment maintenance, support, and emergency repair issues have been solved by remanufacturing technology [1]. For instance, the United States has remanufactured and repaired damaged titanium alloy components of military helicopters, saving 20,000 to 60,000 dollars in comparison with the costs required for replaceing them with new components [2]. Remanufacturing technology conforms to the concept of "energy saving, emission reduction, and green development" in the current world, and it is widely used in construction machinery, machine tool equipment, aviation and aerospace industries, military equipment, and other fields [3].

Currently, electrodeposition, spraying, surfacing, and laser cladding, etc. are typically used as remanufacturing techniques [4-7]. The coatings obtained by electrodeposition and spraying exhibit a low bonding strength with the substrate. Hence, these coatings are prone to large-area peeling during service. In addition, electrodeposition is less repeatable and controllable. Although surfacing welding can obtain coatings with a higher bonding strength, substrate deformation is possible due to the input of excess heat power. As a green remanufacturing technology, laser cladding exhibits advantages of a high repair accuracy, smaller heat-affected zone, higher material utilization rate, and higher interfacial bonding strength.

***Guang-lei Liu**

Ph. D. His research interests mainly focus on the strengthening and toughening of casting alloys and their laser processing modification technology.

E-mail: liugl@ujs.edu.cn; 106409480@qq.com

Received: 2024-03-11; Revised: 2024-07-29; Accepted: 2024-12-05

Hence, it is considered to be the frontier and a promising direction of remanufacturing technology [8]. However, owing to effects of heat transfer and stress-strain relationship in the laser cladding process, the cladding process parameters need to be further controlled; otherwise, improper handling can easily lead to problems such as deformation, micro-cracks [9], and residual tensile stress [10, 11]. Typical solutions to these problems include preheating of the substrate [12], application of an external field during cladding [13], and heat treatment [14]. However, these solutions make the remanufacturing process based on laser cladding more complicated and increase costs slightly. In recent years, some studies have reported [15-17] that laser melting of FeMnSiCrNi memory alloy coatings, which absorbs stress-strain energy through martensitic phase transformation during solidification to reduce the residual tensile stress and microcracks, serves to improve the coating quality [18-20]. Therefore, optimizing the laser cladding process parameters to match the prepared shape memory alloy (SMA) coatings has attracted considerable research.

Compared with other similar methods, response surface methodology (RSM) can be the most important method for laser cladding process optimization as the optimal combination of different process parameters can be obtained through fewer experiments while maintaining a high modeling accuracy [21]. Based on this premise, a mathematical model between the cladding process parameters and SMA coating shaping quality was established by RSM. The model was further optimized by the NSGA-2 algorithm to obtain a new optimized laser cladding method for SMA coating, which provides a reference and guide for the application and development of the laser cladding remanufacturing process.

2 Experimental procedure

Commercially available 304 stainless steel was used as the base material, which was firstly wire-cut into cubes with the dimension of 100 mm×50 mm×10 mm. Subsequently, the surface was polished with sandpapers, cleaned to remove abrasive debris, and dried. Commercially available Fe, Mn, Si, Cr, and Ni powders were used as cladding powders with a purity of 99.99% and a particle size range of 10–50 μm. According to the composition shown in Table 1, the powders were weighed using an electronic balance with a precision of 0.1 mg, and subsequently placed in a vacuum drying oven at 120 °C for 2 h. The dried powder was ball-milled in a YXQM-2L planetary vacuum ball-miller for 2 h, with a ball-to-material ratio of 10:1 and a ball milling speed of 180 r·min^{-1}. Figure 1 shows the powder morphology after ball milling. It can be seen that all kinds of powder particles present irregular shape and with angles, but the dispersion of the particles is good, no obvious agglomeration phenomenon.

In the laser cladding test, a TruDisk 6002 disk fiber laser, with a rated power of 6 kW, an optic fiber diameter of 0.2 mm, and a laser wavelength of 1,064 nm, was used. A KUKA six-axis robot with a positioning precision of 0.05 mm was used as the robotic arm. A 5wt.% polyvinyl alcohol solution was used as the binder, and the powder was pre-pressed on the substrate surface using grooves with dimensions of 100 mm×50 mm×height (height was 0.5, 1, or 1.5 mm). During the cladding process, single-layer multi-channel laser cladding was performed under argon with a purity of 99.9% and a flow rate of 15 L·min^{-1}.

Table 1: Composition of Fe-base shape memory alloy

Element	Si	Mn	Cr	Ni	Fe
wt.%	6	16	9	5	Bal.

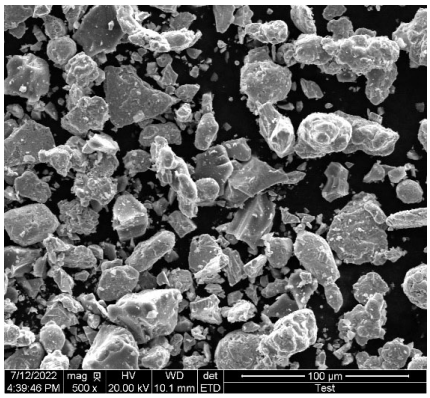

Fig. 1: SEM morphology of Fe-base shape memory alloy powder

In this experiment, four process parameters, namely laser power (P), scanning speed (V), overlap rate (λ), and powder thickness (T), were selected as variables to explore the optimal process parameter pairing for laser cladding [22], as shown in Table 2. According to the previous research results of our research group, a Box-Behnken design (BBD) was employed to establish a total of 29 test schemes with five center points. After the laser cladding was completed, all coating surfaces were probed using the DPT-5 flaw detection reagent, to ensure that the coatings were free of cracks before proceeding with subsequent performance testing. Roughness (Ra) and microhardness (H) were utilized to represent surface quality and mechanical properties of the coatings, respectively.

The three-dimensional morphology of the coating surface was observed using a LEXT OLS4000 laser confocal scanning microscope, and surface roughness was calculated. The hardness of the sample was measured using an FM-ARS900 microhardness tester at a loading load of 300 gf and a loading time of 15 s. The macroscopic morphology of the sample surface was observed using a stereo microscope (Nikon SMZ25, Japan). The cross-sectional structure of the coating was observed with a Zeiss metallographic microscope. The hardness of the sample surface was measured using a TTX-NHT3 nanoindentation hardness tester at a loading load of 100 mN and a holding time of 15 s. The distribution of elements in different areas of the coating was analyzed using an energy-dispersive analyzer (EDS) accessory of an FEI Nova Nano 450 scanning electron microscope (SEM). The electrochemical corrosion test was

carried out on the coating and the substrate separately using the electrochemical workstation CHI760E of Shanghai Chenhua Instrument Co., Ltd. The corrosion medium was selected to simulate seawater (3.5wt.% NaCl), and the corrosion area was 1 cm^2.

3 Results and discussion

3.1 Experimental design and results of RSM

Table 2 shows the specific design scheme and test results using the roughness and microhardness as the target response values.

Table 2: Experimental design and analysis results of response surface method

Experiment No.	Parameter				Response		
	P (W)	*V* (mm·s^{-1})	*λ* (%)	*T* (mm)	*Ra* (μm)	*H* (HV)	Surface morphology
1	1,200	7	50	0.5	8.860	238.12	
2	1,400	6	50	1.5	21.228	233.57	
3	1,200	6	50	1	4.615	271.56	
4	1,400	5	50	1	19.175	242.12	
5	1,200	6	40	0.5	3.977	259.28	
6	1,000	6	40	1	8.122	286.31	
7	1,200	7	40	1	10.865	267.95	
8	1,000	6	50	1.5	13.151	287.86	
9	1,200	6	50	1	10.461	264.43	
10	1,400	6	40	1	9.355	246.23	
11	1,200	6	60	0.5	16.894	264.09	
12	1,200	6	50	1	10.122	263.39	
13	1,200	5	50	1.5	13.974	240.68	
14	1,200	7	50	1.5	15.182	275.25	
15	1,200	5	50	0.5	10.714	259.96	
16	1,200	6	60	1.5	24.637	284.34	
17	1,200	5	60	1	18.846	275.64	
18	1,000	6	60	1	14.527	291.69	
19	1,200	6	50	1	9.156	266.89	
20	1,000	6	50	0.5	9.984	245.64	
21	1,200	7	60	1	14.366	279.43	
22	1,400	6	60	1	24.695	276.34	
23	1,200	6	40	1.5	15.035	255.25	
24	1,000	7	50	1	9.516	275.61	
25	1,400	7	50	1	5.537	249.06	
26	1,000	5	50	1	5.151	284.33	
27	1,200	6	50	1	9.995	263.41	
28	1,200	5	40	1	5.156	263.04	
29	1,400	6	50	0.5	12.812	252.62	

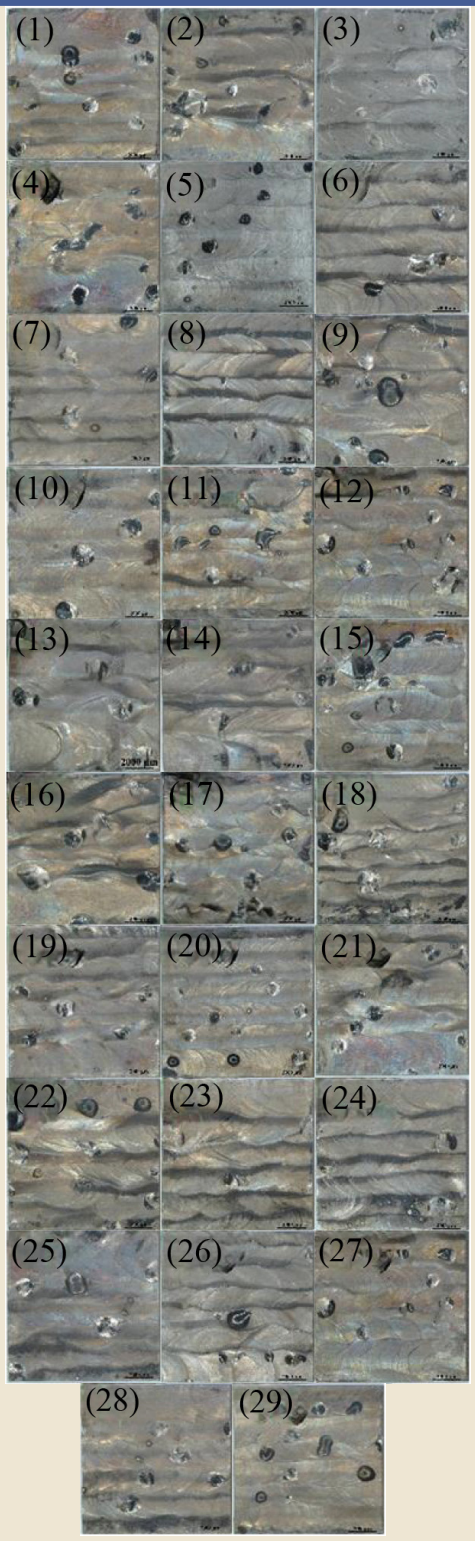

3.2 Response surface modeling

Table 3 shows the results for the variance analysis of the roughness model characterizing the coating quality. The F-value of the roughness prediction model is 19.74, indicating that the model is significant. In Table 3, df represents the degree of freedom, F-value and Pro-Value are the results obtained from the significance test of the model and the coefficient of the model in the analysis of variance, PC represents the sum of squares of each model in the percentage of the total square. A Pro-Value of less than 0.05 indicates that the item in the model is significant; hence, the laser power (P), overlapping ratio (λ), powder thickness (T), interaction items PV, $P\lambda$, $V\lambda$, and quadratic items P^2, λ^2, T^2 are significant. R^2 is 0.9274, indicating that the experimental value is highly correlated with the predicted value. The significance, model coefficients, and missing items of the response model were tested, and the best fitting model was selected on the basis of the fitting analysis. Stepwise regression was adopted to screen and eliminate the insignificant items in the model [23, 24]. Adjusted R^2 and predicted R^2 are 0.8804 and 0.8041, respectively, with a difference of less than 0.2. The Adeq. signal-to-noise ratio is 16.0357 and greater than 4, verifying that the model is reliable and can be used for improving the experimental design. The same method was adopted to optimize and analyze the microhardness model, the results are list in Table 4.

The mathematical model of roughness and microhardness with process parameters is established as follows:

$$\begin{aligned} Ra=&-27.4369-0.027289P+39.01658V-2.73293\lambda \\ &-36.52427T-0.022504PV+0.001117P\lambda \\ &+0.013122PT-0.254725V\lambda+0.000045P^2 \\ &+0.034332\lambda^2+13.71914T^2 \end{aligned} \tag{1}$$

$$\begin{aligned} H=&756.53278-0.190296P-15.10953V-13.53225\lambda \\ &+41.24865T+0.019575PV+0.003091P\lambda \\ &-0.153175PT+28.205VT+1.214\lambda T \\ &-2.91233V^2+0.093877\lambda^2-38.91432T^2 \end{aligned} \tag{2}$$

s. t. $\{1{,}000\le P\le 1{,}400,\ 5\le V\le 7,\ 40\le\lambda\le 60,\ 0.5\le T\le 1.5\}$.

Figure 2 shows the normal distribution of residuals and the comparison between the predicted and experimental values of surface roughness and microhardness. Figures 2(a) and (c) show that the residual values of each response prediction model exhibit a linearly distribution and are uniformly distributed,

Table 3: Variance analysis results of roughness

Source	Sum of squares	df	Mean square	F-value	Pro-value	Significance<0.05	PC
Model	855.02	11	74.25	19.74	<0.0001	Significant	93.04
P	87.22	1	87.22	23.18	0.0002	Significant	9.49
V	6.29	1	6.29	1.67	0.2132	Insignificant	0.68
λ	314.73	1	314.73	83.66	<0.0001	Significant	34.25
T	133.11	1	133.11	35.38	<0.0001	Significant	14.49
PV	81.03	1	81.03	21.54	0.0002	Significant	8.82
$P\lambda$	19.96	1	19.96	5.31	0.0342	Significant	2.17
PT	6.98	1	6.89	1.83	0.1937	Insignificant	0.76
$V\lambda$	25.95	1	25.95	6.90	0.0177	Significant	2.82
P^2	21.32	1	21.32	5.67	0.0292	Significant	2.32
λ^2	79.29	1	79.29	21.08	0.0003	Significant	8.63
T^2	79.14	1	79.14	21.04	0.0003	Significant	8.61
Residual	63.95	17	3.76				6.96
Lack of fit	40.40	13	3.11	0.5278	0.8286	Insignificant	4.40
Pure error	23.55	4	5.89				2.56
Cor total	918.97	28					
Std. Dev.	1.94		R^2	0.9274			
Mean	12.28		Adjusted R^2	0.8804			
C.V.%	15.79		Predicted R^2	0.8041			
PRESS	172.56		Adeq. precision	16.0357			

Table 4: Variance analysis results of microhardness

Source	Sum of squares	df	Mean square	F-value	Pro-value	Significance<0.05	PC
Model	6,866.50	12	591.64	56.34	<0.0001	Significant	97.61
P	2,451.02	1	2,451.02	233.40	<0.0001	Significant	34.84
V	32.18	1	32.18	3.06	0.0992	Insignificant	0.46
λ	728.05	1	728.05	69.33	<0.0001	Significant	10.35
T	273.03	1	273.03	26.00	0.0001	Significant	3.88
PV	61.31	1	61.31	5.84	0.0280	Significant	0.87
Pλ	152.89	1	152.89	14.56	0.0015	Significant	2.17
PT	938.50	1	938.50	89.37	<0.0001	Significant	13.34
VT	795.52	1	795.52	75.76	<0.0001	Significant	11.31
λT	147.38	1	147.38	14.03	0.0018	Significant	2.09
V^2	57.06	1	57.06	5.43	0.0332	Significant	0.81
$λ^2$	592.86	1	592.86	56.46	<0.0001	Significant	8.43
T^2	636.70	1	636.70	60.63	<0.0001	Significant	9.06
Residual	168.02	16	10.50				2.39
Lack of fit	120.35	12	10.03	0.8415	0.6350	Insignificant	1.71
Pure error	47.67	4	11.92				0.68
Cor total	7,034.52	28					
Std. Dev.	3.24		R^2	0.9769			
Mean	264.28		Adjusted R^2	0.9595			
C.V.%	1.23		Predicted R^2	0.9174			
PRESS	600.16		Adeq. precision	27.5866			

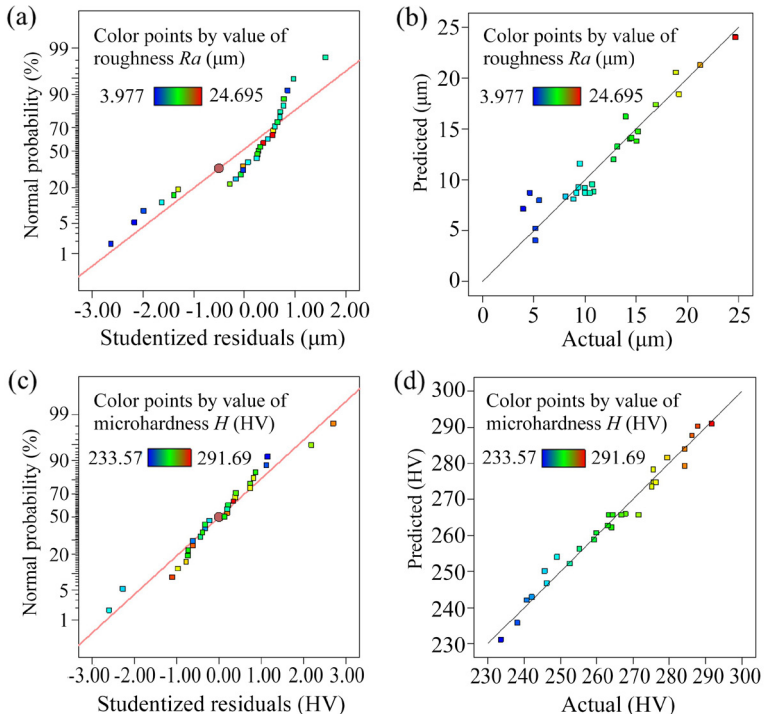

Fig. 2: Residual normal distribution and prediction-actual distribution: (a) and (b) surface roughness; (c) and (d) microhardness

indicating that the models are adaptive. Regarding the comparison between the model predicted values and the experimental values in Figs. 2(b) and (d), the discrete points of surface roughness and microhardness in the plots are concentrated near the diagonal line, which is roughly linear. It indicates that the model's error is small, and both the two response models have a high prediction accuracy and confidence level.

3.3 Effect of process parameter interactions on response values

Effects of interactions among process parameters on the surface roughness of the coating were manifested by 3D surface response and contour lines (Fig. 3). From the analysis on the contribution of each item in Table 3, the surface roughness of the coating decreases in the order of overlapping ratio (λ)>powder thickness (T)>laser power (P)>scanning speed (V). Roughness exhibits an increasing trend under high power-low scanning speed and low power-high scanning speed [Figs. 3(a) and (b)]. This result is related to the fact that an extremely high laser power and an extremely low scanning speed cause excess heat input, resulting in the over-burning of powder and more splash; this in turn easily forms splash pits or residual oxides on the surface and subsequently increases roughness. On the contrary, at an extremely low laser power and an extremely high scanning speed, heat input is insufficient; hence, the powder cannot be completely alloyed. As a result, some powders with a low specific gravity are suspended on the top of the molten pool. After the solidification of the molten pool, the coating exhibits an increased number of surface burrs, and roughness increases. Therefore, under conditions that ensure the powder is completely melted, a small heat input should be selected to prevent over-burning and oxidation of the powder so as to ensure a lower coating roughness. With an increase in laser power, overlapping ratio, and powder thickness, the surface roughness of the coating firstly decreases and then increases [Figs. 3(c)–(h)]. For increasing scanning speed, the coating surface roughness tends to increase at low lap rates and decrease at high lap rates.

The 3D surface response and contour lines in Fig. 4 reveal the effects of interactions among process parameters on the microhardness of the coating. From the contribution analysis of each parameter in Table 4, the microhardness of the coating decreases in the order of laser power>overlapping ratio> powder thickness>scanning speed. With the increase in the laser power, the microhardness of the coating decreases [Figs. 4(a) and (b)]. The microhardness of the coating is higher under a lower power, while the change in scanning speed has a negligible effect on the microhardness. With the increase in the overlapping ratio, the microhardness of the coating firstly decreases and then increases [Figs. 4(c) and (d)]. Coating microhardness with the increase in powder thickness shows a trend of firstly increase and then decrease [Figs. 4(e)–(j)], this is because at first the thickness of the preset layer increases so that the thickness of the alloy layer increases, above the dilution decreases, and with the thickness of the preset layer increases again, the coating oxidation burnout increases, resulting in an increase in the number of coating defects.

In summary, at a laser power range of 1,050–1,250 W, the scanning speed range is 5–7 mm·s^{-1}, the overlapping ratio range is 40%–55%, the powder thickness range is between 0.6 and 1.1 mm, the coating exhibits a lower surface roughness and higher microhardness, demonstrating a better surface quality.

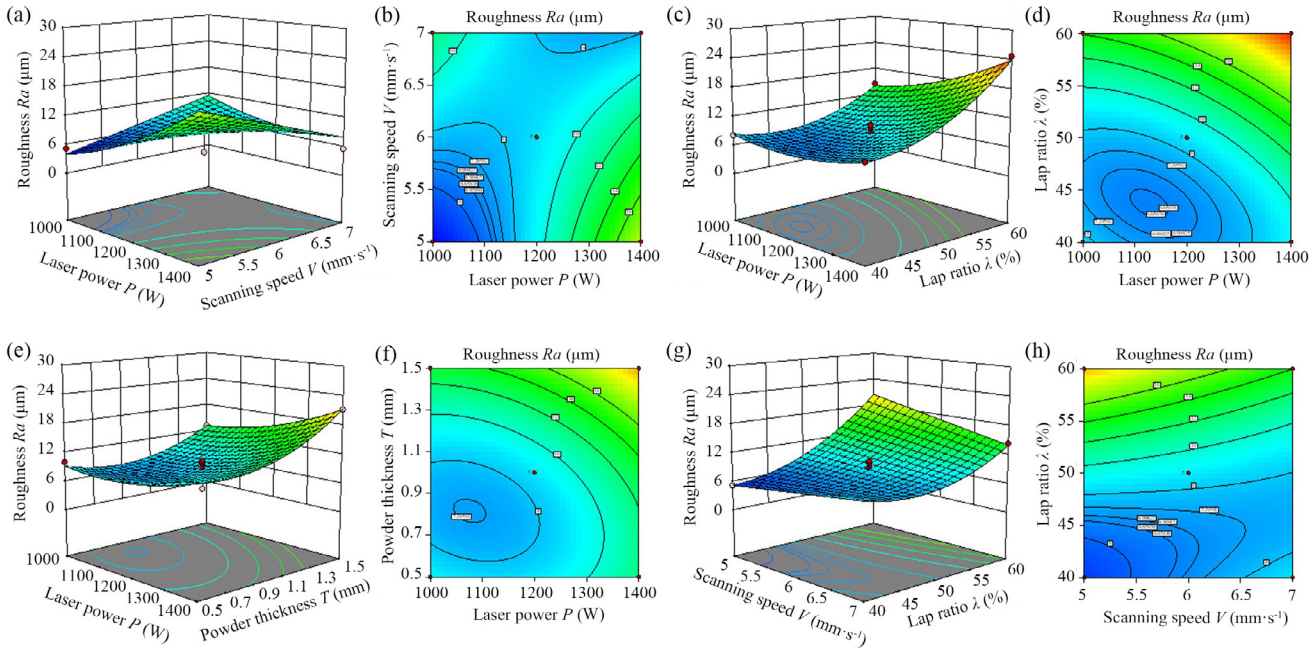

Fig. 3: 3D response surface and contour lines of the influence of process parameter interaction on coating surface roughness: (a), (b) laser power and scanning speed; (c), (d) laser power and lap ratio; (e), (f) laser power and powder thickness; (g), (h) scanning speed and lap rate

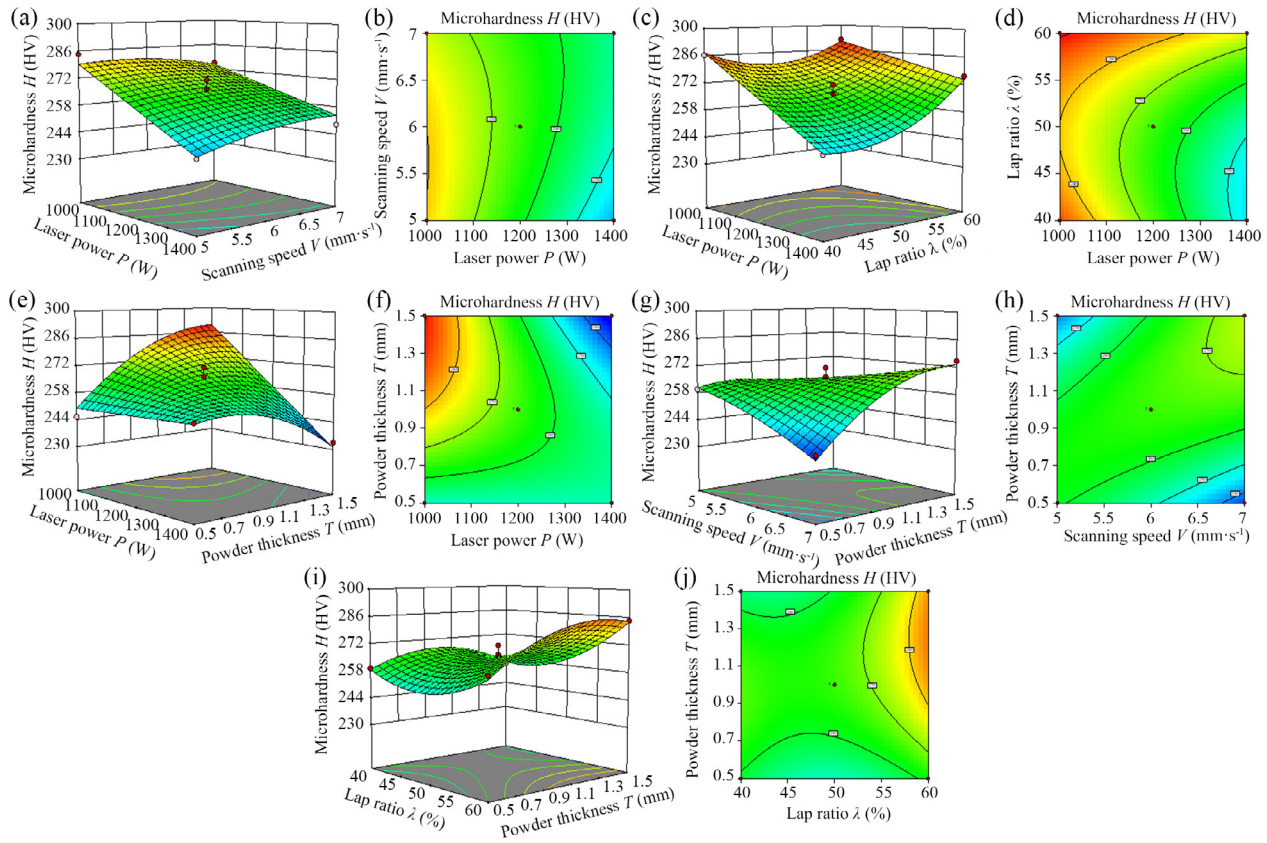

Fig. 4: 3D response surface and contour lines of the influence of process parameter interaction on coating microhardness: (a), (b) laser power and scanning speed; (c), (d) laser power and lap ratio; (e), (f) laser power and powder thickness; (g), (h) scanning speed and powder thickness; (i), (j) lap ratio and powder thickness

3.4 NSGA-2 algorithm optimization

The multi-objective genetic algorithm is based on the theory of evolution, and it is a global optimal search method that simulates the biological evolution process in nature. According to the natural law of the "survival of the fittest", genetic operators (such as selection, crossover, and mutation) are used to iteratively obtain the optimal individual in the evolution process, finally obtaining the globally optimal solution. Among them, the non-dominated sorting genetic algorithm II (NSGA-2) with an elite strategy exhibits advantages of less human intervention, high precision, and high efficiency; hence, it has been widely used for multi-objective optimization and solution [25,26]. Figure 5 shows the flowchart of NSGA-2.

To achieve the goal of minimum surface roughness and maximum microhardness of the cladding layer, the interactions among the four process parameters of laser power, scanning speed, cladding overlapping ratio, and powder thickness, respectively, must be analyzed in depth to clarify the optimal combination. This is shown in Eq. (3):

$$\begin{cases} \min: Ra(P,V,\lambda,T) \\ \max: H(P,V,\lambda,T) \end{cases} \quad (3)$$

Variable value range $\{1050 \le P \le 1250, P \in 10 \times N, 5 \le V \le 7, V \in 0.1 \times N, 40 \le \lambda \le 55, \lambda \in 1 \times N, 0.6 \le T \le 1.1, T \in 0.05 \times N, Ra < 6.5\}$

The optimization conditions of the NSGA-2 genetic algorithm include a crossover probability of 0.9, a mutation probability of 0.1, a population size of 50, and a number of iterations of 100 [27]. The Pareto solution set was solved by Matlab. Figure 6 shows a set of optimal process parameters and predicted response values that satisfy the conditions: a laser power of 1,100 W, a scanning speed of 6.3 mm·s^{-1}, an overlapping ratio of 42%, a powder thickness of 0.65 mm, a roughness of 2.662 μm, and a microhardness of 277.12 HV.

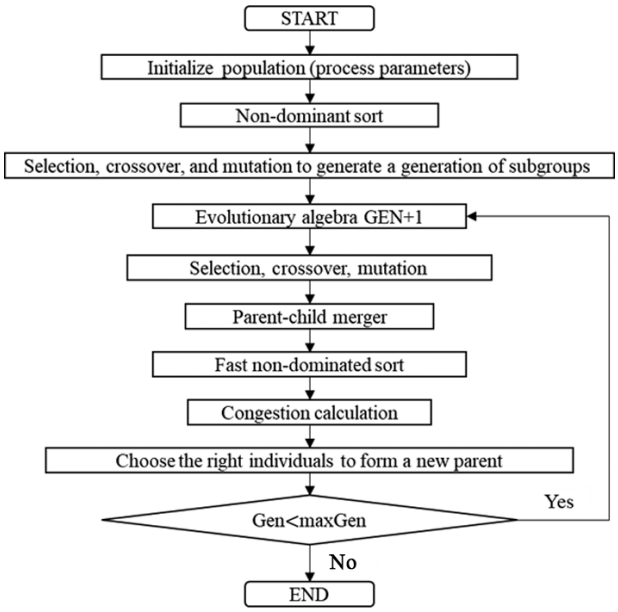

Fig. 5: NSGA-2 algorithm flow

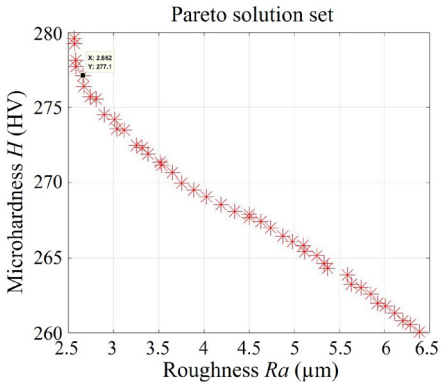

Fig. 6: Pareto solution set results and the position of the optimal solution in Pareto solution set

Table 5: Pareto solution and experimental results

Optimization objectives	Pareto solution	Experimental value	Relative error
Roughness, *Ra* (μm)	2.662	2.781	4.47%
Microhardness, *H* (HV)	277.12	285.34	2.97%

Fig. 7: Coating penetration test results

3.5 Laser cladding process validation and analysis

The FeMnSiCrNi SMA coating was prepared by using Pareto solution set-optimized process parameters. Errors between the model predicted values and actual experimental values for roughness and microhardness are 4.47% and 2.97%, respectively (Table 5). Figure 7 shows the penetration test result of the coatings, and the coating surface does not exhibit deformation and macroscopic micro-cracks.

Figure 8 shows the sectional microstructure of the cladding layer of the sample prepared under the optimized process parameters. Good metallurgical bonding between the coating and substrate is obtained, and defects such as pores and cracks are absent. The structural morphology from the bonding area to the coating surface includes planar crystals, cellular crystals, dendrites, and equiaxed crystals successively, which completely satisfy microstructure standards of laser cladding layers [28].

Figure 9 shows the microstructure of the scanning area in the overlapping and unlapped area of the coating section. As can be seen from Fig. 9, the grains in the unlapped area will form utricular crystals along the opposite direction of the heat flow because the solidification rate is too fast and the degree of subcooling is too small. The microstructure of the overlapping area is mainly dominated by equiaxial crystals due to that the overlapping area undergoes a second heating and melting, which promotes the recrystallization process in the local area. Consequently, the grain growth is restricted, thereby reducing the formation of large grains, and the microstructure of the grains is more fine and homogeneous [29,30]. Figure 10 show the cross-section scanning results for the element distribution of the coating surface. Uniform distributions of Fe, Mn, Si, Cr, and Ni in the overlapped and non-overlapped regions formed by laser cladding are observed, with no obvious segregation.

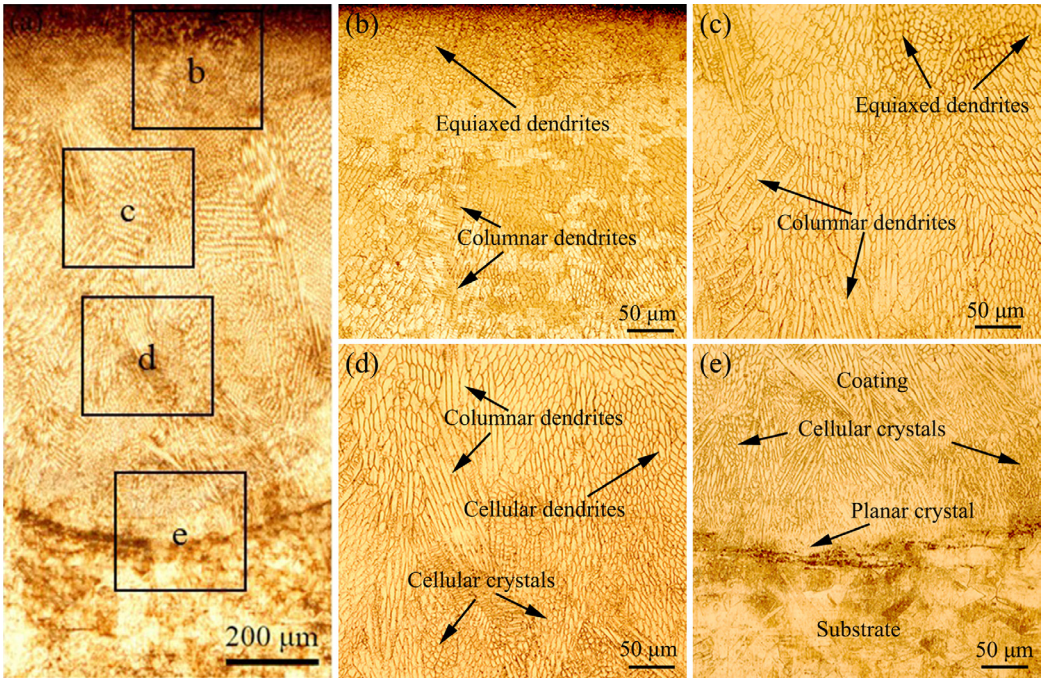

Fig. 8: Coating cross-section microstructure: (a) cross section; (b), (c), (d), and (e) are enlarged views of Areas b, c, d and e in (a), respectively

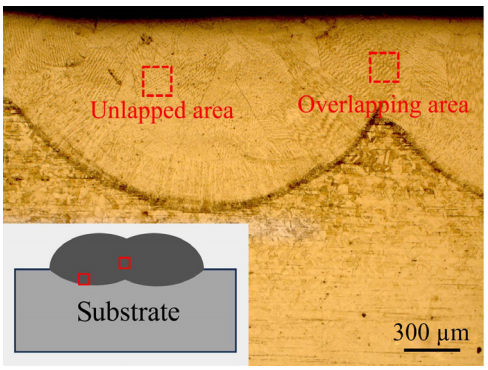

Fig. 9: Microstructure of overlapped and unlapped areas of the coating cross-section

Figure 11 shows the load-displacement curves obtained by the nanoindentation test on the substrate and coating. The maximum indentation depth on the coating is 892.5 nm, which is smaller than the maximum indentation depth on the substrate of 945.9 nm, indicating that the hardness of the coating is greater than that of the substrate. Combined with the nanoindentation test results shown in Table 6, the energy recovery rate and elastic work of the coating are greater than those of the substrate, indicating that the coating exhibits better superelasticity than the substrate. Studies have reported that the higher the elastic deformation energy of the material, the better its performance [31].

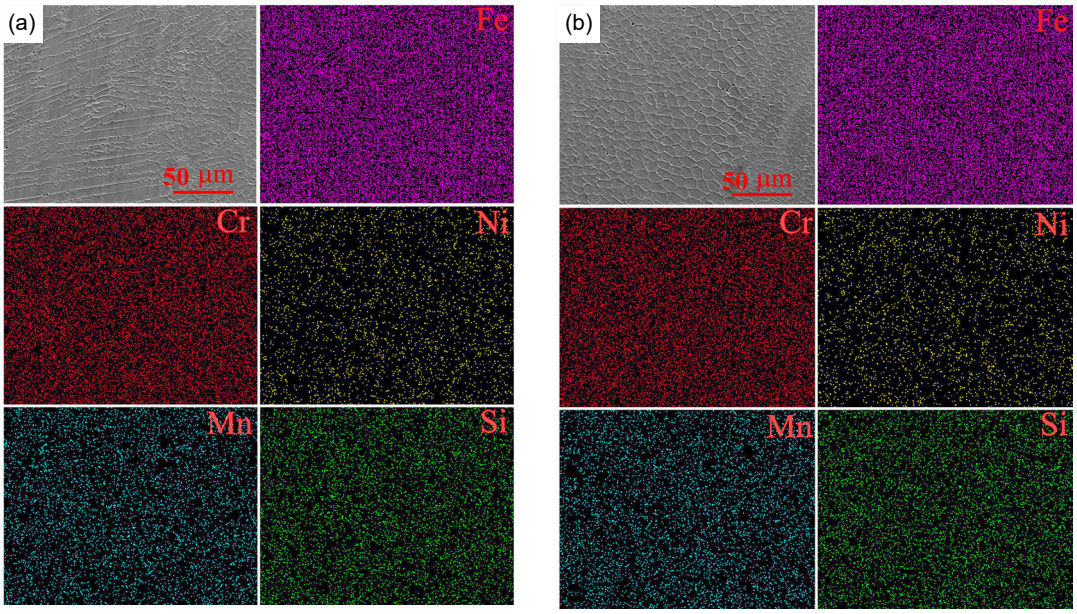

Fig. 10: Distribution of main elements in overlapping (a) and unlapped (b) area of laser cladding coatings

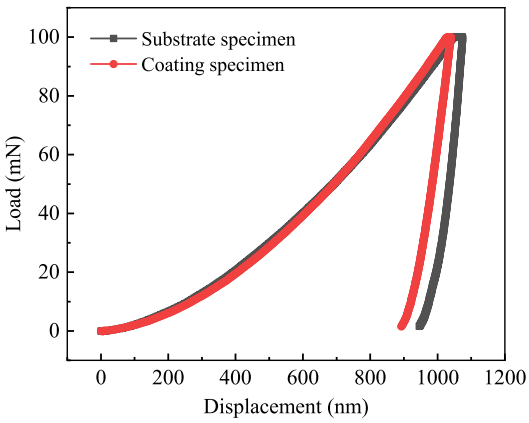

Fig. 11: Nano indentation *P-h* curve

Figure 12 shows the potentiodynamic polarization curves of the substrate and the coating in a 3.5wt.% NaCl solution. According to the data presented in Table 7, the coating has a larger self-corrosion potential (E_{corr}=–0.4754 V), smaller corrosion current density (I_{corr}=8.0359×10^{-6} A·cm^{-2}) and higher impedance (R_p=24,154.83 Ω) compared to the substrate, which indicates the better corrosion resistance of the coating. Meanwhile, compared with the niobium-doped Fe-Mn-Si-Cr-Ni coatings prepared by Zhang et al. [32], the iron based memory alloy coatings prepared in this experiment have higher self-corrosion potential (E_{corr}), little difference in corrosion current density (I_{corr}), and higher impedance (R_p) than the maximum polarization resistance of 5wt.% niobium doped amounting to 7.16±0.7 kΩ.cm^{-2}. It is well known that Cr

Table 6: Nano indentation data of samples

Sample	Maximum displacement (nm)	Microhardness (HV)	Energy recovery rate n_w (%)	Elastic work W_{elast} (PJ)
Substrate	1,074.21	325.23	11.56	4,867.98
Coating	1,029.02	369.90	15.47	5,994.08

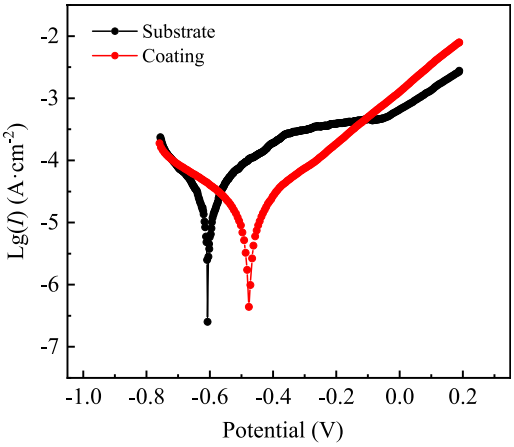

Fig. 12: Polarization curve of cladding layer on substrate in NaCl solution (mass fraction 3.5%)

element is the key element of passivation film, and the addition of Cr element in this experiment (9%) is higher compared to Zhang et al. (4%), so its corrosion resistance is better. This also confirms the high quality of the coating prepared by the process optimization method. After electrochemical corrosion, the corrosion behavior of the iron-based coatings in 3.5wt.% NaCl solution was further investigated by scanning electron microscopy observation. Figure 13 shows the typical corrosion morphology and EDS data of the coating surface. According to EDS data, the abundant C atoms near the grain boundaries tend to interact with Fe and Cr atoms to form $M_{23}C_6$ and M_7C_3 carbides, which leads to a decrease in the Cr content at the grain boundaries and the formation of Cr-poor regions. The corrosion performance of the grain boundary decreases, leading to preferential corrosion that developes as an intergranular corrosion pattern. Due to the intergranular defects, the corrosion solution firstly corrodes and sheds in the intergranular, and then the spreads to the periphery and extends into the iron-based coating. This process results in the peeling off of the coating's surface layer and the formation of typical corrosion pits [33]. The schematic diagram of the corrosion process is shown in Fig. 14. As can be seen from Fig. 14, in NaCl solution, corrosion firstly starts from the surface of the coating, and preferential corrosion occurs due to the reduced corrosion resistance of the grain boundaries, leading to corrosion exhaustion around the grains, and ultimately, the Fe^{2+} is dislodged, resulting in the formation of typical corrosion pits.

Table 7: Corrosion parameter values obtained by polarization curve

Sample	E_{corr} (V)	I_{corr} (A·cm^{-2})	β_a (mv·dec^{-1})	β_c (mv·dec^{-1})	R_p (Ω)
Substrate	−0.6088	2.2233×10^{-5}	0.2941	−0.1686	7,449.51
Coating	−0.4754	8.0359×10^{-6}	0.2672	−0.1673	24,154.83

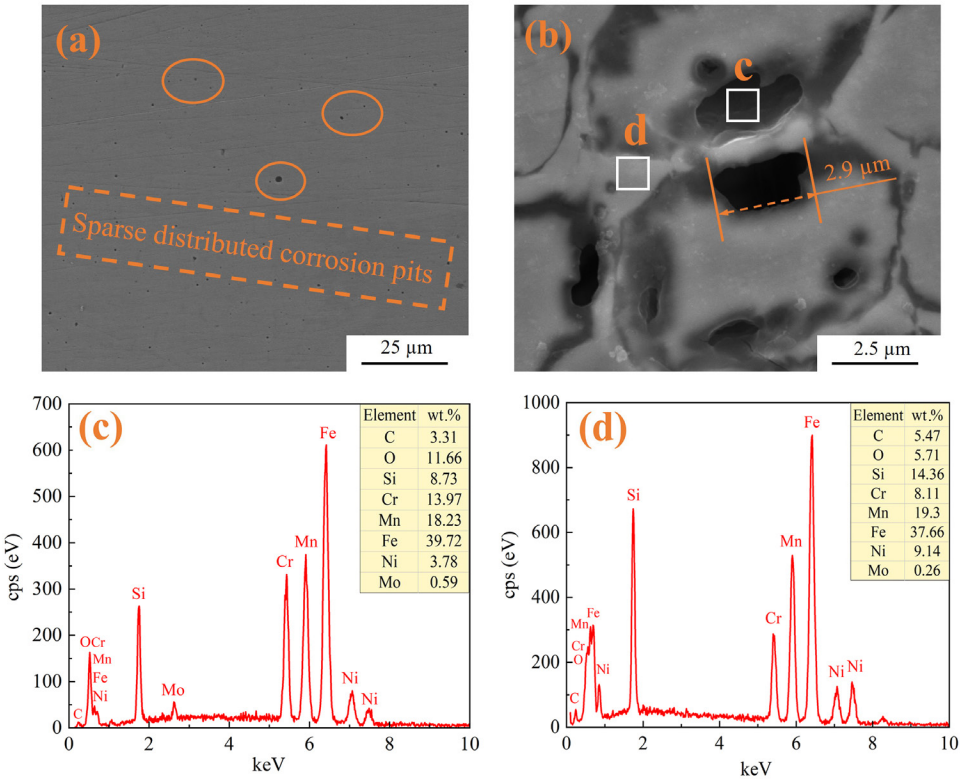

Fig. 13: Low magnification (a) and high magnification (b) microscopic observation of the coating surface after electrochemical corrosion experiments in 3.5wt.% NaCl solution, and (c) and (d) EDS results of the corresponding elements at Points c and d in (b), respectively

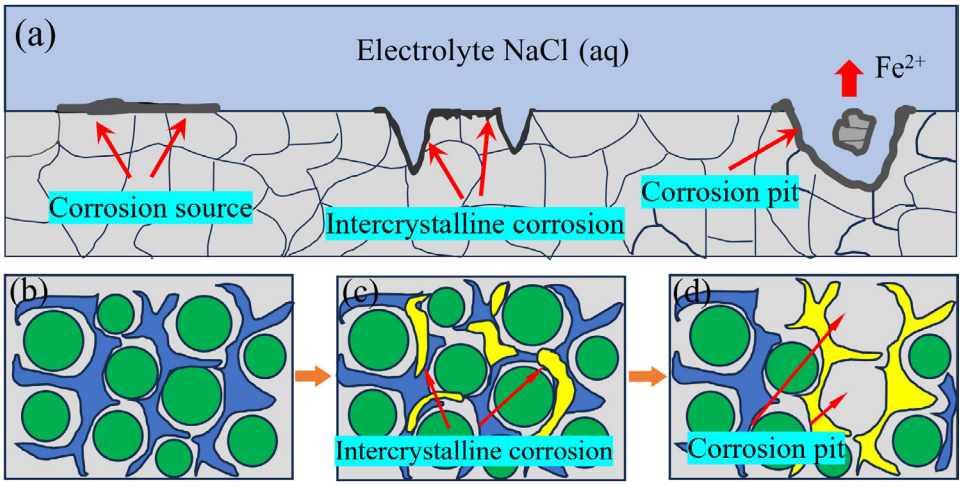

Fig. 14: Schematic diagram of electrochemical corrosion behavior of coatings in 3.5wt.% NaCl solution: (a) cross-sectional corrosion diffusion; (b, c, d) corrosion diffusion on the top surface

4 Conclusions

(1) Based on RSM and NSGA-2, the effects of the synergistic interaction among the laser cladding parameters on the microstructure and properties of coatings can be optimized, so that an accurate mathematical model can be established. It is verified that the error of the established mathematical model is less than 4.5%, indicating its guiding significance in practical engineering applications.

(2) The optimized process parameters for laser cladding of Fe-Mn-Si-Cr-Ni SMA coatings on 304 stainless steel are as follows: laser power 1,100 W, scanning speed 6.3 $mm \cdot s^{-1}$, overlap rate 42%, powder thickness 0.65 mm. Under optimized process parameters, metallurgical bonding is achieved between the coating and the substrate without cracks, pores and segregation of the components. The surface roughness and hardness of the coating are 2.781 μm and 285.34 HV, respectively. Its energy recovery and elastic work are superior to those of the substrate.

(3) Compared with the corrosion results of the substrate in a 3.5wt.% NaCl solution, the coating shows a larger self-corrosion potential (−0.4754 V), a lower corrosion current density (8.0359×10^{-6} $A \cdot cm^{-2}$), and a higher impedance (24,154.83 Ω), which indicates that the coating has better corrosion resistance. By analyzing the morphology of the coated surface after corrosion, it is found that the surface corrosion of Fe-based coatings belongs to minor pitting and intergranular corrosion.

Acknowledgments

The authors are grateful for the financial supports from the National Natural Science Foundation of China-Youth Project (51801076), the Provincial Colleges and Universities Natural Science Research Project of Jiangsu Province (18KJB430009), the Postdoctoral Research Support Project of Jiangsu Province (1601055C), and the Senior Talents Research Startup of Jiangsu University (14JDG126).

Conflict of interest

The authors declare that they have no known competing financial interests or personal relationships that could have appeared to influence the work reported in this paper.

References

[1] Fang Y M, Wei W H, Gong X, et al. Characteristics, connotation and military application of additive remanufacturing technology. Journal of Physics: Conference Series, 2021, 1948(1): 012118.
[2] Zhu S. Flexible additive remanufacturing technology. Journal of Mechanical Engineering, 2013, 49(12): 1–5.
[3] Mei K, Pu Y Z, Di J J, et al. Repair method of key components of imported high precision machine tools based on remanufacturing technology and artificial intelligence technology. 2020 International Conference on Robots & Intelligent System (ICRIS), Sanya, China, 2020: 694–697.
[4] Siddiqui A A, Dubey A K. Recent trends in laser cladding and surface alloying. Optics & Laser Technology, 2021, 134: 106619.
[5] Jia Q Q, Li D Y, Zhang Z, et al. Comparison of oxidation resistance of Al-Ti and Al-Ni intermetallic formed in situ by thermal spraying. Materials Research Express, 2019, 6(9): 096408.
[6] Li X C, Liang H, Zhao Y Z, et al. Microstructure and wear resistance of $AlCrFeNiMo_{0.5}Si_x$ high-entropy alloy coatings prepared by laser cladding. China Foundry, 2022, 19(6): 473–480.
[7] Yuan L, Ding Z Y, Liu S J, et al. Cathodic process of nickel electrodeposition from ammonia-ammonium chloride solutions. Rare Metals, 2023, 42(3): 1061–1066.
[8] Yao Z H, Yao J H, Xiang Q. Research on laser remanufacture technology and application development. China Engineering Science, 2020, 22(3): 63–70.
[9] Luu D N, Zhou W, Nai S M L. Mitigation of liquation cracking in selective laser melted Inconel 718 through optimization of layer thickness and laser energy density. Journal of Materials Processing Technology, 2022, 299: 117374.
[10] Li G Q, Zhu G X, Wang L F, et al. Influence of defocusing amount on temperature and stress field of hollow-ring laser cladding layer. China Mechanical Engineering, 2021, 32(5): 587–593, 599. (In Chinese)

[11] Meng L, Zhao W F, Hou K L, et al. A comparison of microstructure and mechanical properties of laser cladding and laser-induction hybrid cladding coatings on full-scale rail. Materials Science and Engineering: A, 2019, 748: 1–15.
[12] Li Y J, Dong S Y, Yan S X, et al. Surface remanufacturing of ductile cast iron by laser cladding Ni-Cu alloy coatings. Surface and Coatings Technology, 2018, 347: 20–28.
[13] Jiang D, Cui H Z, Song X J, et al. Wear and corrosion resistance of CoCrNi composite coatings by laser cladding. China Foundry, 2022, 19(6): 535–543.
[14] Guo Y X, Shang X J, Liu Q B. Phase transformation of MC/AlCrFeNb3MoTiW high entropy alloys composite coating by in-situ laser cladding. Rare Metals, 2018, 42(8): 807–813.
[15] Liu G L, Xue W C, Cao Y H, et al. Influence of laser shock peening on microstructure and property of Ni60 cladding layer and the combined area of 20CrNiMo alloy. Journal of Laser Applications, 2023, 35(2): 022009.
[16] Tian J Y, Xu P, Chen J H, et al. Microstructure and phase transformation behaviour of a Fe/Mn/Si/Cr/Ni alloy coating by laser cladding. Optics and Lasers in Engineering, 2019, 122: 97–104.
[17] Tian J Y, Xu P, Liu Q B. Effects of stress-induced solid phase transformations on residual stress in laser cladding a Fe-Mn-Si-Cr-Ni alloy coating. Materials & Design, 2020, 193: 108824.
[18] Liu X C, Xu P, Yao L K, et al. Nb reinforced Fe-Mn-Si shape memory alloy composite coating fabricated by laser cladding on 304 stainless steel surface. Journal of Mechanical Science and Technology, 2022, 36(10): 5027–5033.
[19] Su W N, Zhang C, Cui X F, et al. Effect of heat and cryogenic treatments on the microstructure and properties of YF_3 modified NiTi-Si laser cladding coatings. Optics & Laser Technology, 2023, 165: 109614.
[20] Liu C Y, Xu P, Li S B, et al. Evading stress-property tradeoff in a SMA/PZT laser cladding coating via phase transformations. Surface & Coatings Technology, 2022, 436: 128313.
[21] Hashemi S H, Vafaei R, Razavi R S. Statistical-experimental modeling of the effect of process parameters on geometric characteristics of laser cladding of stellite 6 on SS316 using second-order regression. Journal of Materials Research and Technology, 2024, 28: 2727–2739.
[22] Zhang Y, Bai P K, Li Z H, et al. Multi-objective optimization of laser cladding process parameters for Q345B steel. Materials Today Communications, 2024, 39: 108679.
[23] Chaisson T, Lee S, Burns D E. Design optimization of a wind tunnel force balance using stepwise response surface method. Journal of Mechanical Science and Technology, 2022, 36(6): 3071–3079.
[24] Li B X, Wang W C, Zhang X P, et al. Integrating uniform design and response surface methodology to optimize thiacloprid suspension. Scientific Reports, 2017, 7: 46018.
[25] Rahimbakhsh H, Kohansal M E, Tarkashvand A, et al. Multi-objective optimization of natural surveillance and privacy in early design stages utilizing NSGA-II. Automation in Construction, 2022, 143: 46018.
[26] Guo Y R, Shi Q, Guo C M. A performance-oriented optimization framework combining meta-heuristics and entropy-weighted TOPSIS for multi-objective sustainable supply chain network design. Electronics, 2022, 11(19): 3134.
[27] Bu K Z, Zhao Y, Zheng X C. Optimization design of foundation pit engineering above subway tunnel based on NSGA2 genetic algorithm. Journal of Railway Science and Engineering, 2021, 18(2): 459–467. (In Chinese)
[28] Liu Y Y, Yang Y, Chen C. Microstructure and properties of Ni-Ti based gradient laser cladding layer of Ti6Al4V alloy by laser powder bed fusion. Additive Manufacturing, 2024, 79: 103906.
[29] Song H L, Guo C H, Chen L, et al. Effect of microstructure of overlapping regions on the wear/corrosion resistance performance of laser cladded Fe-based amorphous composite coatings. Journal of Non-Crystalline Solids, 2024, 643: 123189.
[30] Bu X Y, Xu X, Lu H F, et al. Effect of overlap rate on the microstructure and properties of Cr-rich stainless steel coatings prepared by extreme high-speed laser cladding. Surface and Coatings Technology, 2024, 487: 131025.
[31] Shi Z P, Wang Z B, Wang J Q, et al. Effect of Ni interlayer on cavitation erosion resistance of NiTi cladding by tungsten inert gas (TIG) surfacing process. Acta Metallurgica Sinica (English Letters), 2019, 33(3): 415–424.
[32] Zhang Q, Xu P, Jiang T, et al. Nb-doped FeMnSiCrNi coatings: Microstructure, phase transformation, shape recovery rate, wear and corrosion resistance. Optik, 2022, 271: 170202.
[33] Xu X, Lu H F, Luo K Y, et al. Mechanical properties and electrochemical corrosion resistance of multilayer laser cladded Fe-based comp osite coatings on 4Cr5MoSiV1 steel. Journal of Materials Processing Technology, 2020, 284: 116736.